Journal of Materials Chemistry A

Water-Enhanced CO_2 Capture with Molecular Salt Sodium Guanidinate

Journal:	*Journal of Materials Chemistry A*
Manuscript ID	TA-ART-05-2024-003037.R1
Article Type:	Paper
Date Submitted by the Author:	21-May-2024
Complete List of Authors:	Evans, Hayden; National Institute of Standards and Technology, Carter, Marcus; National Institute of Standards and Technology Zhou, Wei; National Institute of Standards and Technology, NIST Center for Neutron Research Yildirim, Taner; National Institute of Standards and Technology Brown, Craig; National Institute of Standards and Technology, Center for Neutron Research Wu, Hui; National Institute of Standards and Technology, NIST Center for Neutron Research

Water-Enhanced CO_2 Capture with Molecular Salt Sodium Guanidinate

Hayden A. Evans,[1] Marcus Carter,[1] Wei Zhou,[1] Taner Yildirim,[1] Craig M. Brown,[1,2] Hui Wu[1]**

[1]NIST Center for Neutron Research, National Institute of Standards and Technology, Gaithersburg, Maryland 20899-6102 United States.

[2] Department of Chemical and Biomolecular Engineering, University of Delaware, Newark, Delaware 19716, United States.

ABSTRACT

Solid-state amine absorbent materials, including those containing guanidine derivatives, have received tremendous attention as the world combats the challenges of climate change. Although these materials are attractive for their selective CO_2 capture capacity and fast absorption kinetics, the CO_2 absorption mechanism with such materials can be unclear and differs when H_2O is present. In this work, we present a detailed study on a model guanidine-based crystalline salt, sodium guanidinate ($NaCN_3H_4$), and examine the CO_2 absorption with and without humidity. The simple composition and high crystallinity of $NaCN_3H_4$ and its carbonate capture products allow us to perform ex-situ and in-situ PXRD to identify possible reaction pathways. These results are complemented by detailed thermogravimetric analysis and gas studies to derive holistic mechanistic insight. We determine that $NaCN_3H_4$ exhibits a kinetically controlled CO_2 absorption

profile with an absorption capacity of ≈ 12.3 mmol CO_2/g, assuming a 1:1:1 reaction between CO_2, H_2O, and $NaCN_3H_4$. Importantly, humidity is found to significantly lower the activation energy and increase absorption kinetics of CO_2 absorption as the products Na_2CO_3 and $(CN_3H_6)_2CO_3$ form. Our study demonstrates the advantages and drawbacks of using guanidinate materials for CO_2 capture under flue gas conditions, and provides clarity about how CO_2 capture with similar compounds can be enhanced by humidity.

INTRODUCTION

The increasing atmospheric concentration of carbon dioxide (CO_2) caused by fossil fuel combustion has raised worldwide alarm as the cost of global climate change is felt more acutely each year. In hopes of limiting the future effects of climate change, carbon capture is acknowledged as one of the necessary carbon abatement strategies,[1–3] with complementary research being conducted on utilizing the captured CO_2.[4–9] However, to efficiently capture CO_2, an economical sorbent material must meet as many of the following requirements as possible: strong CO_2-binding affinity, rapid sorption kinetics, high capacity, strong selectivity for CO_2, simple regeneration with minimal energy input, long-term stability, chemical safety, and low cost. While a material possessing all these characteristics remains undiscovered, and may prove elusive, sustained efforts over the past two decades have identified numerous classes of sorbents that exhibit many of these desired attributes. These sorbents include metal-organic frameworks (MOFs), zeolites, alkali metal oxides, amine containing materials, etc.[3–16]

Amongst solid-state materials for CO_2 capture, amine-based sorbents such as poly(ethylenimine) (PEI) functionalized porous silica absorbents are well-known and have attractive attributes.[8,17,18] These attributes include being scalable, selective for CO_2, and showing

utility in various CO_2 capture systems with industrial sources.[18–21] However, while most of the reported studies on PEI materials focus on the carbon capture performance of the materials, most do not provide mechanistic investigation on what or how species form during CO_2 absorption.[8,18] This fundamental deficit in understanding prevents rational material development for long-term cyclability prospects, and to date, certain PEI-based materials still have ambiguous CO_2 chemisorption mechanisms with irreversible side reactions.[22–25] As such, interest in related materials that have attractive CO_2 capture attributes is ongoing.

One such amine-related class of materials of interest for CO_2 capture are those containing the organic moiety guanidine and its derivatives,[26] which have shown CO_2 capture cyclability, strong basicity, and structural modifiability.[27–32] Currently, most reported guanidine-based sorbents exist in ionic liquid form or in an aqueous or alcohol solution, and although these liquid systems capture CO_2 well, they also have limitations generally associated with liquid-phase sorbents. This includes the substantial energy required to regenerate captured media (aqueous heat capacity constraints) and the inherent volatility of the small molecular constituents in the solution phase.[8,26,27]

Solid-state guanidine-based compounds for CO_2 capture also exist but predominantly as guanidinylated organic derivatives on silica.[33–36] These materials are compelling as they have shown faster absorption kinetics compared to their liquid counterparts and, in certain cases, have also demonstrated superior stability and regeneration conditions compared to poly(ethylenimine) (PEI) functionalized silica absorbents.[33,35] However, the solid guanidine-based compounds have incomplete CO_2 absorption mechanism understanding akin to the polymeric amine systems. This is due to the systems' complex nature, including poor crystallinity, unknown absorption products, and insufficient experimental probes. Theoretical work has helped address these issues and

provided clarity about the potential configuration of possible guanidine – CO_2 complexes,[37,38] indicating that guanidine is an absorbent molecule with stronger CO_2 interactions than established amine-based systems.

This study aims to provide context for CO_2 capture with solid-state guanidinates[39] by examining a model compound, sodium guanidinate ($NaCN_3H_4$). By doing so, we strive to clarify how such materials fundamentally behave when undergoing CO_2 fixation. In this work, we have examined $NaCN_3H_4$ under conditions compatible with combustion flue gas (0.1 bar to 1 bar CO_2 pressure at temperatures ≤ 383 K (110 °C)) and reveal how and why humidity is advantageous for reliable CO_2 chemisorption. Our results on CO_2 capture in humidity-limited and humidity-rich conditions with $NaCN_3H_4$ provide mechanistic information to guide future design of guanidine-materials.

EXPERIMENTAL

Synthesis of $NaCN_3H_4$

Guanidine (CN_3H_5) and sodium guanidinate ($NaCN_3H_4$) were prepared using the method detailed in our previous study.[39] Briefly, a stoichiometric amount of Na metal (freshly cut) and guanidinium carbonate (Sigma Aldrich, 99%) (2:1 molar ratio) were used for the synthesis of solid guanidine. The NaH-CN_3H_5 white powder mixtures were milled using a Fritsch Pulverisette 7 planetary mill‡ at 200 rpm for 10 min. After milling, the mixtures were stored in a He-filled glovebox for further structural and property characterizations. To form the final $NaCN_3H_4$, the mixture must be heated to 330 K for ≈ 5 minutes (under a dry atmosphere).

Sievert closed-system gas absorption studies

CO_2 absorption under 0.1 bar - 1.0 bar pressure in a closed cell was characterized on a custom Sieverts-type apparatus, described previously.[40] Various temperatures (between 300 K and 383 K) were tested to determine the appropriate reaction temperature, and pressure changes were monitored as an indication of reaction over long periods of time. Carbon dioxide gas used for experiments was from Roberts Oxygen with extra dry grade (99.8%).

Thermogravimetric analysis (TGA)

TGA measurements with simultaneous differential scanning calorimetry (DSC) were conducted using a Netzsch STA 449 *F1 Jupiter* TGA-DSC instrument under anhydrous CO_2 flow (30 ml/min flow rate) with He gas as the protective gas that we identify as "humidity-limited" conditions. The sample was sealed in an Al crucible with a pierced lid to allow for the penetration/release of gas. As a result, the sample was briefly exposed to air through the pinhole when it was transferred onto the TGA sample stage.

TGA/DSC experiments under "humidity-excess" CO_2 flow were conducted by flowing the anhydrous CO_2 stream through a homemade dewpoint generator fed into the TGA through a gas line heated at 373 K (100 °C). The heated line was used to prevent water vapor condensation within the gas line. The flow rate was kept at 30 mL/min, the same conditions as during humidity-limited experiments. The water content that CO_2 can carry from the dewpoint generator was tested for an appropriate dewpoint temperature so that there would be no water condensation in the gas line blocking the flow pathway in the TGA. More moisture can be generated by higher dewpoint temperatures, but this required a higher CO_2 flow rate to avoid partial water condensation in the gas line. The required higher flow would cause the TGA apparatus to fail to operate under an overpressure condition. To maintain the same flow rate as in the dry CO_2 flow condition and to

prevent overpressure, the input water vapor content set by the dewpoint was fixed for all measured temperatures. Considering the temperature range studied in our TGA experiment, i.e., 368 K – 383 K (95 °C – 110 °C), the final tested optimum operational condition corresponds to a ≈ 10 % relative humidity at 373 K (100 °C). Since the relative humidity decreases/increases when the setting temperature in TGA increases/decreases, the actual relative humidity of the gas stream in TGA would be ≈ 6.8 % - 8 % at (105-110) °C and ≈ 12 % at 95 °C. We estimate a 0.5 % uncertainty in these values.

Ex situ powder diffraction

Ex situ powder X-ray diffraction (PXRD) patterns were taken on samples sealed in glass capillaries (from a He atmosphere glovebox) using a Rigaku X-ray diffractometer with a Cu K_α source. Data were collected at room temperature over the diffraction angle 2θ range of 5° - 70° with a step size of 0.02°. All X-ray data were analyzed using TOPAS.[41]

In situ powder diffraction

In situ high-resolution synchrotron powder X-ray diffraction (SPXRD) data were collected at Beamline 17-BM at the Advanced Photon Source at Argonne National Laboratory. The temperature of the capillary sample was achieved using an Oxford Cryosystems Cryostream 800 calibrated for the capillary geometry. Scattered X-rays were measured by a PerkinElmer amorphous-Si flat panel 2-dimensional (2-D) detector. The calibrated wavelength for the measurements was 0.45171 Å. For humidity-limited CO_2 experiments, one side open quartz capillaries (Hampton-Research, 1 mm outer diameter) were attached to a custom valve-based dosing sample holder and dosed with the necessary pressure of CO_2 gas. For humidity-excess CO_2

experiments, a continuous flow setup was used (available at 17-BM), where a CO_2 stream was first bubbled through a vial of room temperature water and then flowed over the sample at 5 standard cubic centimeters per minute (SCCM). All SPXRD 2-D data were reduced using GSAS-II[42] and analyzed using TOPAS.[41]

RESULTS

The results section is divided into two overarching CO_2 capture experimental categories: one where humidity is limited (humidity-limited, HL) and one where humidity is in excess (humidity-excess, HE). Based on prior work on metal guanidinates, it was appreciated that guanidinates are hygroscopic and form hydroxides readily upon encountering H_2O.[39,43] This hydroxide formation proves essential for CO_2 capture, but for experiments that illustrate HL conditions, great care was still taken to prevent air (H_2O) exposure of samples prior to testing. However, some level of air exposure was unavoidable during experiments where CO_2 flowed over samples even with anhydrous CO_2 sources.

We note that although minute levels of water are likely introduced via flowing HL CO_2 experiments, the limited humidity hinders overall CO_2 absorption and kinetics when compared to CO_2 absorption with HE conditions. As we explain schematically in the discussion section, the CO_2 absorption mechanism with $NaCN_3H_4$ is stoichiometrically dependent on water to promote the formation of carbonate products and increase intermediate product formation/diffusion. A consequence is that efficient and predictable CO_2 absorption is readily achieved within hours under HE conditions, whereas, for HL conditions, CO_2 absorption takes tens of hours and involves detrimental side reactions.

Humidity-limited CO_2 capture experiments

Sievert absorption measurement results under humidity-limited conditions

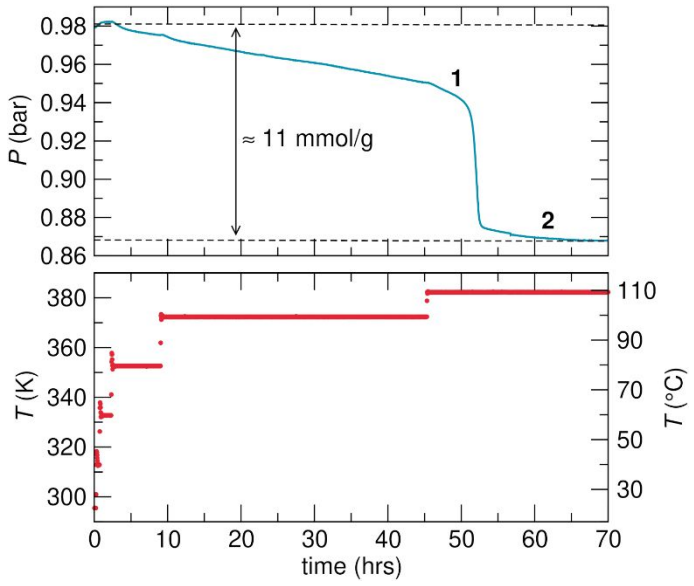

Fig. 1. Humidity-limited Sievert experiment with $NaCN_3H_4$. (top) CO_2 absorption pressure change profile for $NaCN_3H_4$ with an initial ≈ 1 bar CO_2 pressure and (bottom) corresponding temperature range profile of the experiment. Numbers **1** and **2** in the top panel refer to where subsequent experiments were stopped and ex-situ PXRD samples were isolated. The ex-situ diffraction pattern analysis is described in the humidity-limited ex-situ PXRD section.

To establish the fundamental absorption behavior between $NaCN_3H_4$ and CO_2, anhydrous CO_2 static gas absorption experiments over various temperatures were conducted. The experiments entailed exposing $NaCN_3H_4$ to a known molar quantity of anhydrous CO_2 in a custom Sievert apparatus (see experimental section) and monitoring the change of pressure of CO_2 as temperature was increased and held for certain periods (Fig. 1 and Fig. S1, S2, S16).† Given the closed system of the Sievert apparatus, the CO_2 stream was confidently established as anhydrous within the limits of gas purity provided by the gas supplier (see experimental section).

Fig. 1 shows that an initially constant pressure of CO_2 began to decrease as the temperature of the system was increased stepwise above 353 K (80 °C) over the course of ≈ 45 hours. After the temperature was increased to ≈ 383 K (110 °C), with an apparent hour-long induction period, a large decrease in pressure was seen (absorption of CO_2). The total decrease in pressure amounts to a CO_2 absorption quantity of ≈ 11 mmol CO_2 / g of sample.

Thermogravimetric and kinetic analysis under humidity-limited conditions

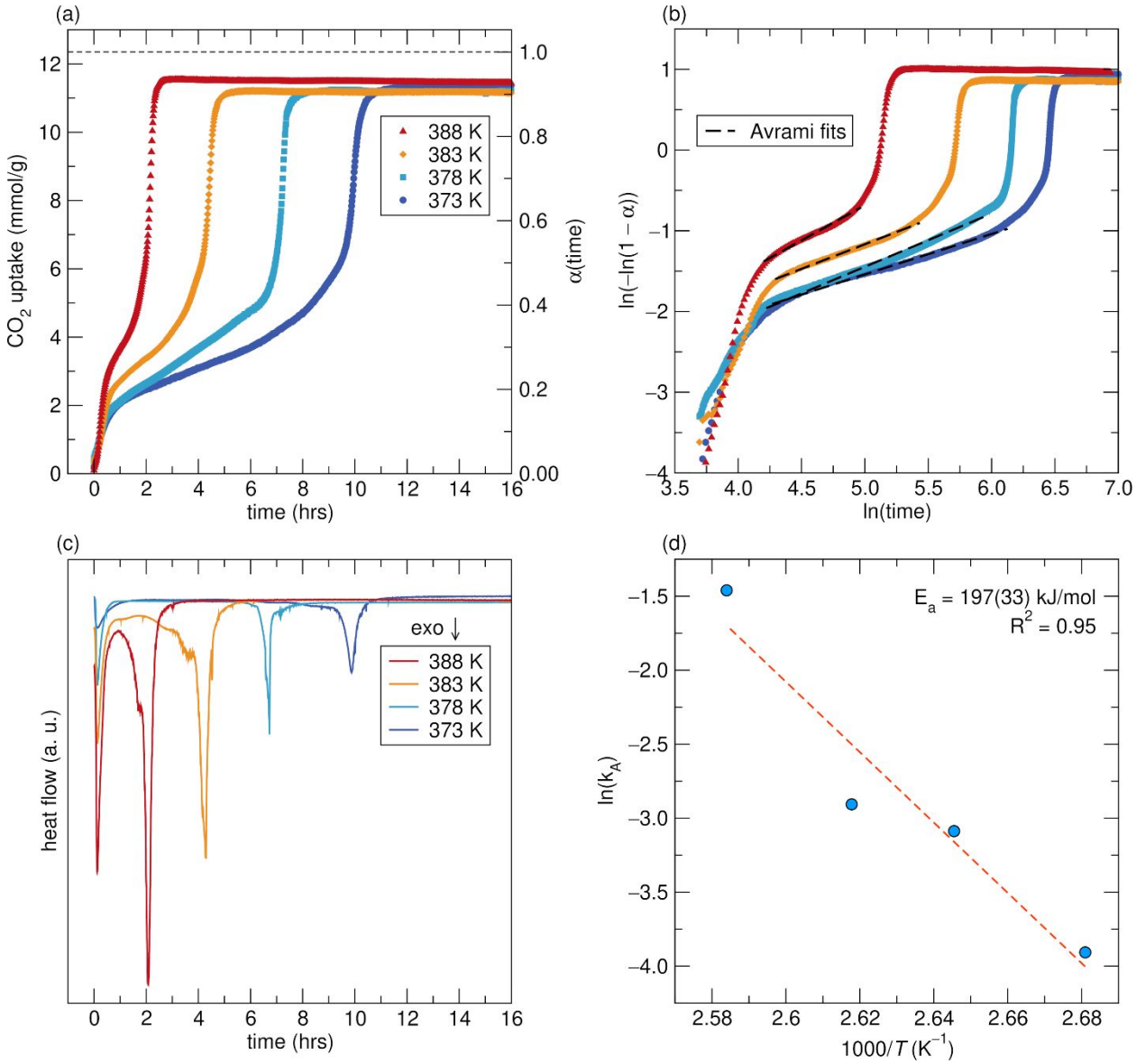

Fig. 2. TGA measurement results under humidity-limited conditions. a) TGA humidity-limited CO_2 uptake results of $NaCN_3H_4$ at various temperatures monitored for ≈ 16 hrs. The dashed line indicates a 1:1:1 reaction between CO_2, H_2O, and $NaCN_3H_4$ corresponding to the theoretical CO_2 uptake capacity of 12.345 mmol·g^{-1}. The reaction fraction α(t) at time, *t*, was calculated by normalizing the observed CO_2 uptakes against the theoretical CO_2 uptake (12.345 mmol/g). b) Avrami plots to derive Avrami exponents (*n*) at different reaction stages; only the induction period fit is shown. Values from pre- and post-induction Avrami fits can be found in Table S1. Legend from panel a) applies to b) and c) Differential scanning calorimetry (DSC) results at different temperatures. d) Arrhenius plot of reaction rate vs $1/T$ for the induction stage. The linear fit line was used to obtain activation energy (E_a). Values in parentheses indicate 1-σ.

To understand the kinetic variation in HL CO_2 absorption with temperature, TGA/DSC measurements were conducted with flowing CO_2 between 373 K – 398 K (100 °C – 115 °C.) The results are shown in Fig. 2. It was established in a prior pyrolysis study of $NaCN_3H_4$,[39] (as well as in Fig. S12 and Fig. S13)† that no phase change or material degradation of $NaCN_3H_4$ occurs in the 373 K – 398 K temperature range under He gas, and as such, all mass and energy change events observed are related to CO_2 absorption.

However, given the nonzero amount of H_2O present during the flowing CO_2 experiment, the estimated values of CO_2 absorbed in mmol/g shown in Fig. 2 are based on two experimental approximations: 1) the sample weight recorded in the glove box was considered as the weight of $NaCN_3H_4$, neglecting potential H_2O scavenged by $NaCN_3H_4$ during handling (glove box levels were consistently beneath 3 ppm H_2O); and 2) the CO_2 uptake in mmol was estimated based on the observed mass gain but consists of both CO_2 and any moisture from the flow gas stream and handling of the DSC sample pan at the instrument. These assumptions likely produce a slight

overestimation of the CO_2 absorbed, and accordingly, we found it prudent to focus more on the shape of the absorption profiles to derive mechanistic and kinetic information rather than the absolute amount absorbed.

Consistent with the HL CO_2 absorption Sievert study (Fig. 1), a notable feature of the TGA profiles of $NaCN_3H_4$ under HL conditions is the existence of prolonged induction periods (Fig. 2a) prior to rapid absorption. The TGA isothermal curves between 373 K to 388 K (100 °C to 115 °C) show that it takes ≈ 10.5 hours to ≈ 2.5 hours, respectively, to achieve the maximum uptakes upon heating, and that these timescales appear largely dependent on the variation in induction times (≈ 9.5 hours at 373 K, ≈ 1.5 hours at 388 K). For all temperatures, a rapid absorption event over ≈ 1 hour was consistently observed after the induction period. As the observed TGA profiles under HL conditions are quite complicated (Fig. 3) and likely party to multiple reactions occurring simultaneously, the Johnson-Mehl-Avrami (referred to here as "Avrami") analysis (equation 1)[13,44,45] and its double-logarithmized form (equation 2) were used for analyzing the intricate kinetic chemisorption profiles under isothermal conditions. This analysis is regarded as most appropriate for systems that are multistaged[13,44–46] and have proven useful for deriving the kinetic parameters at different reaction regimes. The equations are:

$$\alpha(t)=1\text{-}\exp[-(k_A t)^n] \quad (1)$$

$$\ln\ln\frac{1}{1-\alpha(t)} = n\ln t + n\ln k_A \quad (2)$$

where k_A is the Avrami kinetic rate constant, n is the Avrami exponent, t is the reaction time, and $\alpha(t)$ ($0 < \alpha < 1$) is the fraction of chemical reaction at time t.

Fig. 2b shows the plot of $\ln\ln\frac{1}{1-\alpha(t)}$ vs. $\ln t$, where the n and k_A are obtained from the slope and the intercept of the linear fit during the induction period (all fit values listed in Table S1, alongside the additional region fits in Fig. S17† which were omitted from Fig. 2b for clarity). In the slow induction range $0.1 < \alpha < 0.4$ - 0.5 for all measured temperatures, n's are less than 1, which suggests a slow growth of the reaction nuclei of the temporal products and indicates a diffusion-controlled reaction.[47] In the rapid absorption stage (0.4 - $0.5 < \alpha < 1$) for all temperatures, the n's were determined to be > 3, indicating that three-dimensional growth occurs concurrently with the formation of the final products, which is also reflected by the strong exothermic peaks observed in the same time range (0.4 - $0.5 < \alpha < 1$) in the DSC data at various temperatures (Fig. 2c). We note that there is also an initial CO_2 absorption ($\alpha < 0.1$) as shown in Fig. 2a (and evidenced in the continuous pressure drop at 373 K in Fig 1.), likely due to the initial CO_2 chemisorption at the particle surface, without requiring long-range diffusion, which may contribute to the exothermic peaks in the initial reaction stage ($\alpha < 0.1$) (Fig. 2c).

The absorption duration and the estimated Avrami rate constants (k_A) in the induction periods ($0.1 < \alpha < 0.4$ - 0.5) are temperature dependent (Fig. 2b and Table S1), confirming that diffusion of chemical species in the system is the rate-limiting step for HL conditions. Assuming the temperature dependence of the kinetic rate (k_A) in the induction follows the Arrhenius equation, we can construct an Arrhenius plot (Fig. 2d) and derive the activation energy (E_a) from the slope of the fit. The derived E_a in the induction period under HL flowing CO_2 conditions is approximately $E_a = 197 \pm 33$ kJ/mol. We will compare this value to the HE CO_2 absorption values in the discussion section and provide context about how slow water diffusion in the system engenders sluggish reaction kinetics.

Lastly, the time required in the rapid absorption stage ($0.5 < \alpha < 1$) is similar for all the temperatures, consistent with their similar magnitude of Avrami rate constant, i.e. $k_A \approx (2 - 6) \times 10^{-3}$ min^{-1} from 373 K to 388 K (100 °C to 115 °C) (Table S1). Combined with the exothermic DSC peaks in this stage, it appears that the kinetics of the rapid absorption is dominated by the thermodynamic driving force of more stable product formation.

Ex situ diffraction under humidity-limited conditions

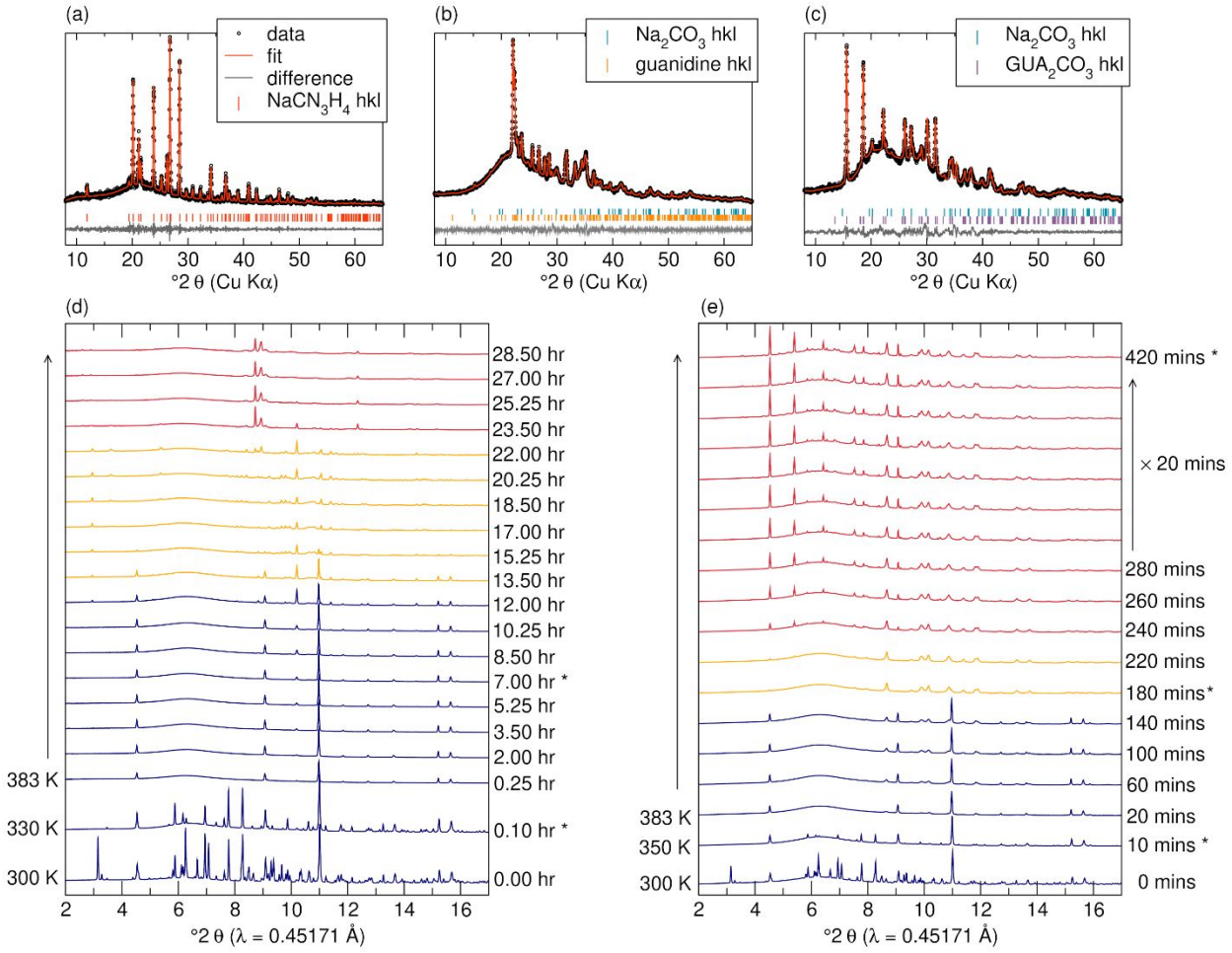

Fig. 3. Diffraction results from HL conditions. (a – c) Pawley fitting of ex-situ samples. (a) Pristine $NaCN_3H_4$ prior to exposure. (b) Stage **1** from Fig. 1 (after induction) showing Na_2CO_3 and solid guanidine (CN_3H_5) present. (c) Stage **2**

from Fig. 1 (after rapid absorption) showing Na_2CO_3 and $(CN_3H_6)_2CO_3$ (labeled as GUA_2CO_3 in Fig.). (d and e) In situ HL CO_2 experiments with NaC_3H_4. [APS, 17-BM]. The vertical arrow on the temperature axis of the graphs indicates where temperature was held at 383 K. (d) Static anhydrous CO_2 exposure (1 bar) monitored for ≈ 28.5 hours. CO_2 was introduced at 300 K and heated under static CO_2 pressure. (e) Flow HL CO_2 (1 bar) exposure monitored for 420 minutes (7 hours). CO_2 was introduced at 300 K and heated under flowing CO_2. The patterns in both (d) and (e) have been colored into three main periods observed via powder diffraction 1) amorphization and existence of NaOH (blue) 2) intermediate reaction period (orange) 3) major product isolation (red). Certain patterns, denoted with * were Rietveld fit to show product isolation, and are presented in the ESI S3 – S7.† Note: in d and e that the initial pattern of $NaCN_3H_4$ reflects the initial state of the as-prepared sample (NaH-guanidine non-homogenous mixture) before the necessary annealing ≈ 330 K to homogenize and transform to the known pristine monoclinic phase of $NaCN_3H_4$ [see Fig. S11]†.[39] Sample remains as a white powder from start to finish during adsorption.

To further understand the chemical reactions associated with the pressure change profile seen in Fig. 1 and TGA experiments shown in Fig. 2, room temperature ex situ lab X-ray diffraction (XRD) patterns were collected on pristine $NaCN_3H_4$ and quenched products from two significant stages of absorption of CO_2 under HL conditions (Fig. 3a – 3c). These stages of quenching were: **1** (Fig. 3b), at the end of the hours-long induction phase (prior to rapid CO_2 absorption), and **2** (Fig. 3c), after rapid CO_2 absorption. At the end of the induction phase crystalline guanidine (CN_3H_5) and sodium carbonate (Na_2CO_3) were present, whereas after the rapid CO_2 absorption, crystalline $(CN_3H_6)_2CO_3$ and Na_2CO_3 existed as the major crystalline products (approximate phase fraction of 2 to 1 $(CN_3H_6)_2CO_3$ and Na_2CO_3.

Ex situ laboratory XRD experiments, though sometimes less favored than in-situ experiments, sometimes have advantages for understanding reaction mechanisms. In this case, interrupting the absorption/reaction process and cooling the samples to room temperature provided an opportunity to observe hidden components of the reaction mixture that are unseen during in situ

experiments. Specifically, crystalline guanidine was observed in the ex-situ sample at the end of the induction phase of HL CO_2 absorption. This phase will not be observed via in-situ PXRD at 383 K (110 °C) given guanidine is liquid at this temperature above 323 K (50 °C).

In situ diffraction under humidity-limited conditions

In situ synchrotron diffraction experiments were performed to monitor the emergence of crystalline phases as CO_2 was absorbed under conditions resembling both the Sievert and TGA HL conditions. Specifically, in situ synchrotron diffraction experiments were conducted under static anhydrous CO_2 conditions (mimicking static anhydrous CO_2 Sievert conditions), as well as with flowing HL CO_2 at 383 K (110°C) (mimicking HL TGA-flow conditions). Select diffraction patterns from each experiment are shown in Fig. 3d and 3e and illustrate differences between the underlying absorption mechanism and the crystalline products that form as a result. Rietveld refinement of select patterns can be found in the SI (Figs. S3 – S7).

The results of the static CO_2 conditions are shown in Fig. 3d. For this experiment, ≈ 25 mLs of CO_2 at 1 bar were available to be reacted with ≈ 10 mg of $NaCN_3H_4$ at 383 K (see experimental section). As can be seen, even though $NaCN_3H_4$ scavenged a small amount of H_2O (forming NaOH), tens of hours were still needed for crystalline CO_2 products to form. The observed reaction progresses in two main steps: In step one, $NaCN_3H_4$ begins absorbing CO_2 and loses crystallinity by 383 K, leaving NaOH as the only observable crystalline phase under 1 bar of CO_2 for nearly 10 hours (the melting point of NaOH is ≈ 600 K). Step two is between 10.25 hours and 22 hours and involves additional product formation (Na_2CO_3 and unidentified phases) until $(CN_3H_6)_2CO_3$ forms in minimal amounts (as identified from Rietveld fits, SI Figs. S3 – S5).

The data supports the hypothesis that the loss of crystallinity of $NaCN_3H_4$ seen in the initial stages of the reaction is a result of CO_2 absorption. In general, the amorphization is likely exothermic. As our DSC shows no related heat event in this temperature range under a He atmosphere (Fig. S12)†, the amorphization then coincides with the CO_2 absorption. However, in the present study under CO_2 atmosphere such an amorphization would also be convolved with the 1st exothermic event observed in the DSC spectra of the CO_2 absorption (Fig. 2c). The same loss of crystallinity occurs in the HE experiments.

During the product formation step between 10.25 hours and 22 hours, there is difficulty in assigning all CO_2 absorption products from PXRD due to their low crystallinity. However, based on Sievert experiments, which suggest ≈ 11 mmol/g uptake of CO_2 occurs over the course of > 40 hours of absorption, we believe CO_2 is being incorporated via some reaction with the guanidine backbone absent of H_2O, forming a predominantly amorphous product. As the time frame in the in-situ XRD does not extend to the total Sievert experiment, we also understand that we may not observe the final stages of CO_2 absorption (Fig 1).

The static HL CO_2 experiment is contrasted by the HL flow CO_2 experiment (Fig 3e), which illustrates that CO_2 absorption under flow conditions progresses more rapidly towards carbonate products. It is worth noting that the two HL reactions (static CO_2 and flow CO_2) are similar at the initial stages, where above ≈ 350 K, NaOH diffraction peaks remain as the only observable phase. This indicates again that $NaCN_3H_4$ is quickly reacted/made amorphous as the system absorbs CO_2. However, compared to the static CO_2 exposure, the flowing CO_2 experiment shows after just ≈ 120 min (≈ 2 hours) of reaction, Na_2CO_3 crystallizes, followed by the crystallization of GUA_2CO_3 starting at 420 mins (4 hours). The ESI contains the Rietveld phase analysis of select patterns (denoted in Fig. 3 with *) of the flowing HL CO_2 experiment. The

analysis indicates that at the end of CO_2 absorption, Na_2CO_3 and GUA_2CO_3 are the predominant crystalline phases formed. However, given the limited humidity, parasitic side reactions still occur and produce unknown phases.

The two HL in situ diffraction experiments confirm that small amounts of H_2O present during CO_2 absorption with NaC_3H_4 enhance and accelerate crystalline carbonate product formation. The diffraction patterns also confirm the suspicion that any H_2O present provides a more favorable kinetic path to forming GUA_2CO_3, which we now discuss as the key to carbonate product formation within the system.

Humidity-Excess CO_2 Capture Experiments

Given the nature of the Sievert experiments, we cannot perform analogous HE experiments like those conducted under anhydrous conditions. However, HE CO_2 absorption flow TGA (Fig. 4 and Fig. S14)† and in-situ synchrotron experiments (Fig. 5) illustrate the nature of CO_2 absorption with $NaCN_3H_4$ under HE conditions.

TGA under humidity-excess conditions

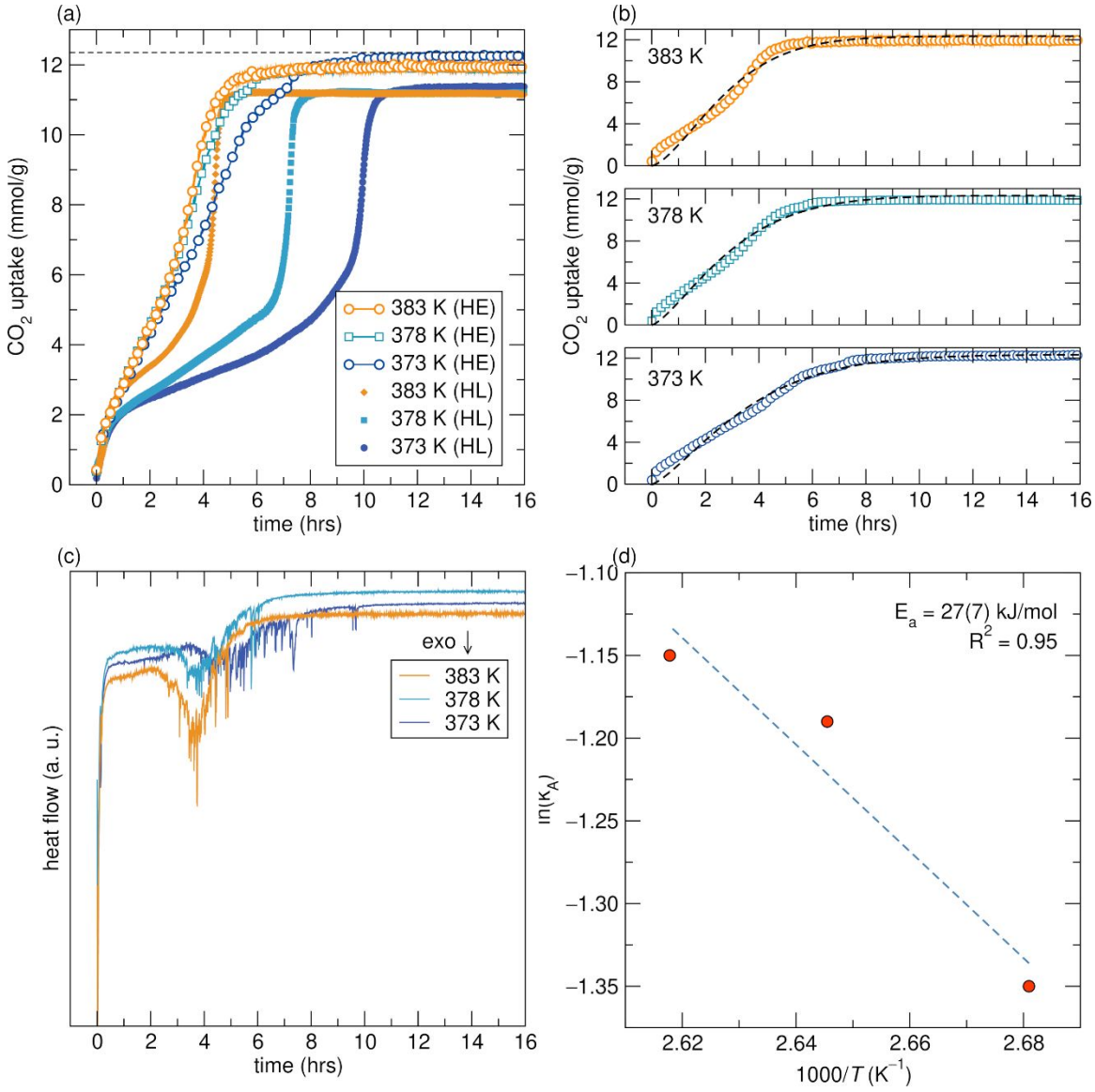

Fig. 4. TGA results and analysis from humidity-excess CO_2 flow conditions. a) Humidity-excess (HE) CO_2 uptakes of $NaCN_3H_4$ with the fixed relative humidity input of approximately 10% at 373 K (100 °C). The corresponding CO_2 uptakes at humidity-limited (HL) conditions presented in Fig. 2(a) are also plotted for ease of comparison. b) Avrami kinetic model fits for the three temperatures shown in panel (a) with fractional-order (n) at different reaction stages. The n and k_A values derived from fitting are listed in Table S2; c) Differential scanning calorimetry (DSC) results obtained during the runs shown in Fig 4a. d) Arrhenius plot of reaction rate vs $1/T$ for the three temperatures measured and the derived activation energy.

Fig. 4a and 4b illustrate the TGA heating profiles and analysis of HE $NaCN_3H_4$ samples. Fig 4a shows HL runs for comparison. What can be quickly noted is that the induction periods in the HE CO_2 uptake profiles are considerably shorter than those seen in HL conditions. It is also seen that the continuous absorption of CO_2 in HE conditions aligns with the continuous exothermic events over the broader time range in DSC spectra (Fig. 4c), compared to the singular exothermic peak in the rapid absorption stage observed under the HL CO_2 conditions (Fig 2c).

Interestingly, the kinetics of the HE absorption were enhanced for all measured temperatures, but the impact of excess humidity proved less significant at higher temperatures. This effect is potentially caused by two convolved factors: i) the limitation of our homemade dewpoint setup (see experimental section) to provide 10% relative humidity (RH) above 373 K (the input RH was fixed as 10% at 100°C, but at 110 C became 6.8% RH) and ii) that the induction period is a thermally activated process where increasing temperature alone can boost diffusion and reaction kinetics. Regarding the mass gain observed, as 383 K is 10 K above the vaporization temperature for H_2O (at 1 atm), we can also be relatively confident that any H_2O uptake results from carbonate formation and not the continual uptake of H_2O. This assumption is supported by the observation of no additional mass change during the 383 K HE TGA run for 6 hours in humid CO_2.

As was done for HL CO_2 TGA data, Avrami modeling using Eq. 1 was used to directly fit the wet CO_2 uptake curves, with the fits shown in Fig. 4b. The average Avrami exponent n derived from fitting for all measured temperatures is found to be between 1 and 1.5, with the complete list found in Table S2 (alongside k_A values). Additionally, a pseudo first-order kinetic model was used to fit these curves, which generated similar and reasonable conclusions to the Avrami model (Table

S2 and Fig S15). These results ultimately reflect the simpler reaction kinetics in the HE conditions compared to the multiple-staged reactions in the HL conditions.

From the Arrhenius plot fitting of $\ln k_A$ vs. $1/T$ of the HE conditions (Fig. 4d) between 373 K and 383 K, we find that E_a = 27 ± 7 kJ/mol. This value of *Ea* for the HE conditions is dramatically lower than the Ea = 197 ± 33 kJ/mol obtained for the induction periodic under HL conditions for the same temperature range. As shown in Fig 4a, direct comparison of the HE CO_2 uptake curves with their HL counterparts strongly suggests that the effect of H_2O in CO_2 streams dramatically changes the CO_2 uptake profile, shortening the induction period.

In situ diffraction under humidity-excess conditions

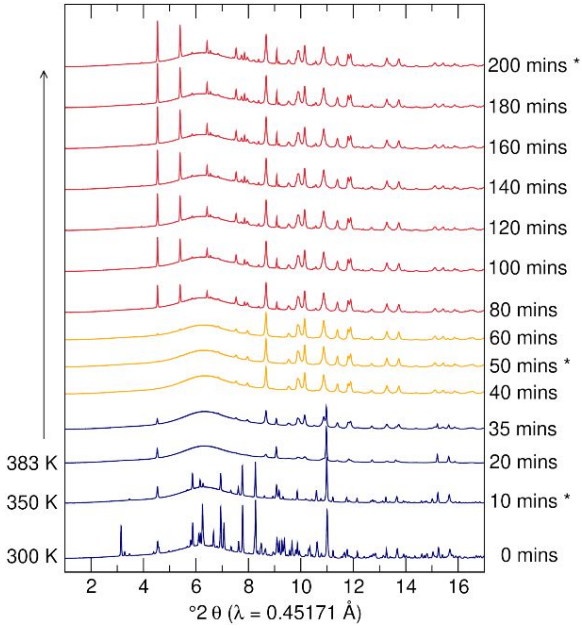

Fig. 5. Select diffraction patterns from the humidity-excess in-situ diffraction experiments [APS, 17-BM]. Certain patterns denoted with * were Rietveld fit to show product isolation and are found in the ESI S8 – S10.† Additionally, we note that the initial pattern of $NaCN_3H_4$ reflects the initial state of the as-prepared sample (NaH-guanidine non-

homogenous mixture) before the necessary annealing ≈ 325 K to homogenize and transform to the known pristine monoclinic phase of $NaCN_3H_4$ [Fig. S11]†.[39]

In situ HE SPXRD experiments reveal the fast reaction pathway between CO_2/H_2O and $NaCN_3H_4$ as crystalline carbonate products form. This contrasts the HL flow in situ PXRD experiment, which proved slower in addition to displaying minor side reactions with the guanidine backbone giving unidentifiable peaks. The in situ HE diffraction data is shown in Fig. 5 (Rietveld refinements in SI Figs S8 – S10), where select diffraction patterns illustrate the reaction course from 300 K to 380 K over 200 mins under flowing humid CO_2 (5 cc per min, bubbled through H_2O at 300 K). Summarized, the as-prepared sample becomes the pristine $NaCN_3H_4$ phase by 350 K, followed by the retention of crystalline NaOH (20 mins, 383 K). NaOH crystallinity then diminishes as Na_2CO_3 forms (between 35 mins and 60 mins), where during the 40 min to 60 min period, Na_2CO_3 is found to be the major crystalline phase. During the 35 min to 60 min period, $(CN_3H_6)_2CO_3$ crystallization occurs and continues to approx. 200 min.

As we examine in the discussion section, guanidine is a likely intermediate species that forms as protons are sequestered from the available H_2O. However, as guanidine is liquid at 383 K, it is challenging to definitively claim what reactions occur from these in situ diffraction experiments. Given the existence of additional diffraction peaks unattributable to Na_2CO_3 between 40 min and 60 min of the reaction, as well as in the final patterns, there are likely other intermediate phases forming. For example, additional reactions could include CO_2 and H_2O forming small quantities of carbonic acid (H_2CO_3), facilitating an additional pathway for protonation of guanidine and the creation of $HCOO_3^-$ anions. However, between 80 min to 200 min, Na_2CO_3 and $(CN_3H_6)_2CO_3$ are the major crystalline products and given the continual increase in intensity of

$(CN_3H_6)_2CO_3$ diffraction peaks during this period, we posit that the formation of $(CN_3H_6)_2CO_3$ is rate limited by the protonation of guanidine. Lastly, we will note that the diffraction observations (as a function of time) align very closely with the CO_2 absorption profile seen for the HE TGA results at 383 K (Fig. 4a). This suggests that the full theoretical ≈ 12.3 mmol/g sequestration of CO_2, which depends on the simultaneous absorption of H_2O, can be achieved under flowing humid CO_2 conditions (based on the formula described in the discussion section).

For added context, we have also shown that $NaCN_3H_4$ works under simulated flue gas (85/15 N_2/CO_2, HE) and closely mimics the CO_2 uptake profile of the material with HE CO_2. There is a slight delay in CO_2 uptake relative to HE CO_2, but the slopes of the uptakes are nearly identical. This data can be found in the ESI, Fig. S19.†

DISCUSSION

Reaction Mechanism

Taking into consideration everything observed from Sievert analysis, TGA, DSC, and the evolution of crystalline phases observed via ex-situ and in-situ XRD studies under humidity-limited and -excess conditions, we propose a stepwise CO_2 chemisorption framework for $NaCN_3H_4$. This is shown in Scheme 1 and comprises four key reaction steps. We include a further breakdown of the scheme under humidity-limited and excess conditions, illustrating how H_2O either feeds or starves the kinetics of carbonate product formation. However, it is noted that as side reactions occur more readily during the HL conditions, aspects of this scheme will not capture the unidentified non-crystalline intermediate products. Our results support the existence of this mechanistic framework under the experimental conditions of the present study most confidently

when H_2O is present in excess and represents the main reaction leading to the majority of the products.

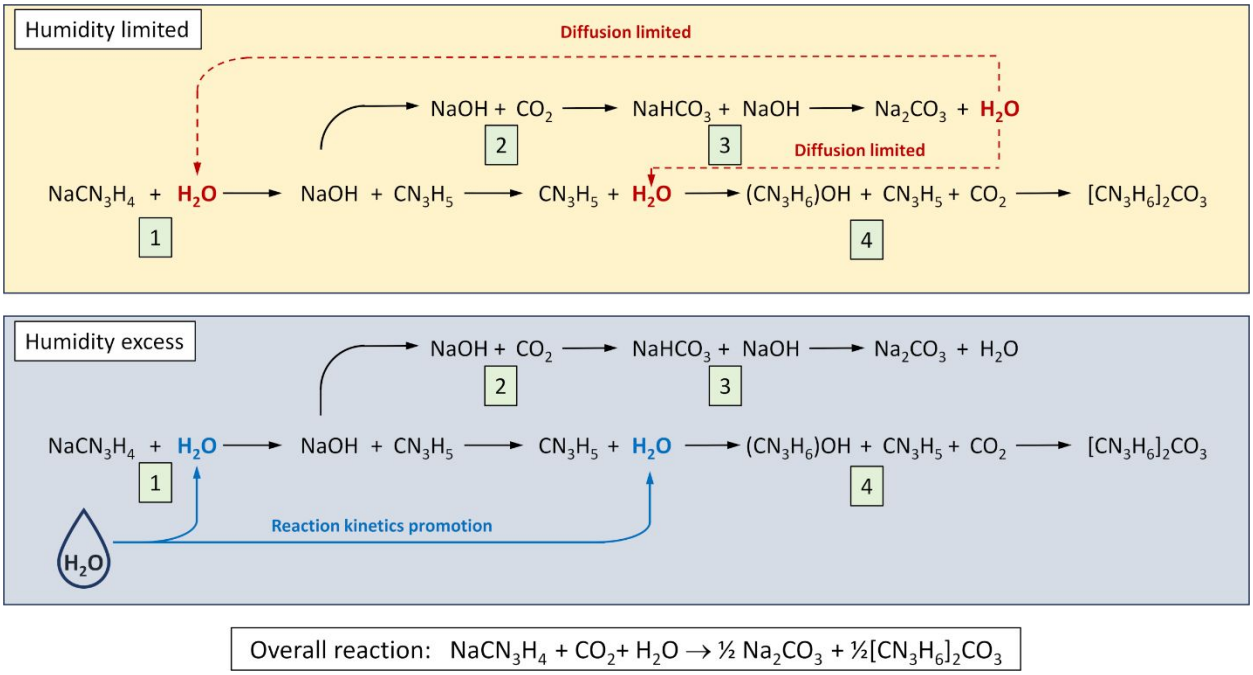

Scheme 1. The schematic reaction mechanism for CO_2 capture by $NaCN_3H_4$ in humidity-limited and -excess conditions. The initial H_2O within the sample begins the formation of NaOH and guanidine (reaction 1), which initiate the later key reactions (2, 3, and 4) needed to form the carbonate products Na_2CO_3 and $(CN_3H_6)_2CO_3$.

Under HL conditions, Scheme 1 (humidity limited, top panel) illustrates how H_2O diffusion through the system governs reaction kinetics and the products formed. In step (1), we assume that some amount of H_2O is present within the system, which can react with $NaCN_3H_4$ into equal amounts of neutral guanidine and NaOH. This proposed step is supported by the initial in-situ and ex-situ PXRD patterns (Fig. 3 and Fig. 5).

The newly formed NaOH can react with CO_2 to form sodium carbonate, and the guanidine can react with H_2O and CO_2 to progress towards $(CN_3H_6)_2(CO_3)$. As is evident from the in situ studies, reactions (2) and (3) that form Na_2CO_3 appear to be the favored pathway reactions under

HL conditions, with pathway 4 forming crystalline $(CN_3H_6)_2CO_3$ only occurring at the later stages of reaction (SPXRD Fig 3b). Given that two equivalents of H_2O are necessary for reactions 2 and 3 (one equivalent to form intermediate $NaHCO_3$ in reaction 2, and the other to form the NaOH used in reaction 3), the limited water in the system is quickly consumed (or evaporated), and its absence stalls the entire reaction. It would therefore appear that the limited H_2O and its diffusion through the system is the cause of the long induction periods observed under HL conditions. In the ESI, we provide a more detailed description of this progression with a mathematical kinetic description of this process (Scheme S1).

To further comment on how the induction period is exaggerated in H_2O-starved systems, we must appreciate the role neutral guanidine may play. Guanidine is highly hygroscopic similar to NaOH,[48] and we speculate that during the formation of NaOH and guanidine in step 1, some amount of guanidinium hydroxide (CN_3H_6OH) forms and even participates in alternate reactions to path 3, complicating our mechanistic understanding. To date, there is no reported crystal structure of the solid CN_3H_6OH. Many structural characterizations of hydrated guanidinium systems in solution indicate that the guanidinium ion ($CN_3H_6^+$) is a weakly hydrated cation and has no recognizable hydration shell, suggesting that a long-range ordered structure for hydrated guanidium ions would be difficult to observe.[49–51] Indeed, we did not identify crystalline CN_3H_6OH from our diffraction studies, but the formation of the crystalline product $(CN_3H_6)_2CO_3$ (Fig. 3b and Fig. 5) indicates that the reaction intermediates guanidine and CN_3H_6OH are likely participants of reaction 4.

The largely featureless in situ SPXRD patterns observed during the induction period in HL conditions (Fig. 3), especially under static CO_2 conditions, also make it difficult to comment on the exact nature of the system when H_2O is limited. It is possible that unexpected side reactions

proliferate as H_2O becomes scarce. Hypothetically, we can speculate that some short-range temporal structures such as carbamates may also exist as carbon dioxide and guanidine react during water-starved induction. This may also contribute to the extremely prolonged time for carbamates to convert to bicarbonates or carbonates, and where such carbamate species would impact the final absorption products. For example, in the ESI, we provide an experiment utilizing a lower pressure of CO_2. Specifically, under the same static HL conditions as shown in Fig. 1, but with only 0.1 bar CO_2 available for the same system volume, we found that after a lengthy induction period, the sample decomposed and did not undergo rapid CO_2 absorption (Fig. S16)†. This experiment shows that the instability of the intermediates at high temperatures may prompt the system to enter a non-recyclable state if there is limited H_2O.

The constraints on reaction rate seen in HL conditions are largely circumvented during HE conditions. This is illustrated in Scheme 1 (humidity-excess, bottom panel). Our in situ SPXRD and flowing HE TGA experiments demonstrate the benefit of excess H_2O. Specifically, they show how excess H_2O helps to bypass kinetic CO_2 capture bottlenecks and provides necessary H_2O to react with, and likely generate, reaction sites (based on the Avrami analysis). In combination, the increased reaction sites, and H_2O available for reaction dramatically reduces the observed induction period and the activation energy of the system. From a thermodynamic perspective, excess H_2O also appears to suppress side reactions, promoting the formation of the intermediates NaOH, guanidine, and CN_3H_6OH needed for unhindered formation of Na_2CO_3 and $(CN_3H_6)_2CO_3$. This is also supported by the less intense but continuous exothermic events seen in DSC over a broader period under HE CO_2 capture conditions.

Lastly, we note that in a model system such as $NaCN_3H_4$, some detrimental side reactions still occur even in excess humidity. As many of these amine systems are touted as capable of

recyclability, there is evidence that this is a pervasive issue that needs further attention. In situ spectroscopic investigation such as FTIR or Raman, for example, may be well suited to better understand and identify exact side reactions. We hope that our mechanistic study here provides needed context on how H_2O can be useful for future material design of anionic anime systems for CO_2 capture, but requires careful consideration. Specifically, we believe that this information will assist scientists on how best to promote the CO_2 capture mechanism to encourage maximum carbonate product formation.

CONCLUSIONS

We have described how the model solid-state guanidinate absorbent, sodium guanidinate ($NaCN_3H_4$), captures CO_2 under flue gas relevant conditions (0.1 bar - 1 bar, ≤ 383 K (110°C)). Importantly, we have described how water proves essential to reliable and maximum CO_2 capture by promoting fast crystallization of carbonate products. Combined with detailed gas absorption studies, TGA, DSC, and ex/in-situ X-ray structural analysis under static and flowing gas conditions, we provide evidence of the humidity enhanced CO_2 chemisorption mechanism for this material. Moisture both mitigates the diffusion-limited reaction stages and drives carbonate product formation as H_2O and CO_2 incorporate into the system. We believe our mechanistic insight into how humidity dramatically impacts CO_2 sequestration in this model compound can help guide future guanidinate based material design. The CO_2 capture process described here also shows how a system such as $NaCN_3H_4$ has merits in comparison to other systems in high humidity conditions, as predictable and stable carbonate products (Na_2CO_3 and GUA_2CO_3) can be fed back into a cyclic process (see Fig. S18).† However, this system also shows hallmarks of other amine systems, or chemisorption systems in general, where even in optimum conditions detrimental side reactions can prevent complete recyclability.

ASSOCIATED CONTENT

Electronic Supplementary Information

Detailed PXRD structural studies and additional TGA absorption data. This material is available free of charge *via* the Internet at http://pubs.acs.org.

AUTHOR INFORMATION

Notes and references

‡ The identification of any commercial product or trade name does not imply endorsement or recommendation by the National Institute of Standards and Technology.

Corresponding Author

*Hayden Evans, NIST Center for Neutron Research, National Institute of Standards and Technology, Gaithersburg, Maryland 20899-6102, United States. Email: hayden.evans@nist.gov

*Hui Wu, NIST Center for Neutron Research, National Institute of Standards and Technology, Gaithersburg, Maryland 20899-6102, United States; Email: huiwu@nist.gov

Authors

Hayden A. Evans, NIST Center for Neutron Research, National Institute of Standards and Technology, Gaithersburg, Maryland 20899-6102, United States. https://orcid.org/0000-0002-1331-4274

Marcus Carter, NIST Center for Neutron Research, National Institute of Standards and Technology, Gaithersburg, Maryland 20899-6102, United States.

Wei Zhou, NIST Center for Neutron Research, National Institute of Standards and Technology, Gaithersburg, Maryland 20899-6102, United States. https://orcid.org/0000-0002-5461-3617

Taner Yildirim, NIST Center for Neutron Research, National Institute of Standards and Technology, Gaithersburg, Maryland 20899-6102, United States. https://orcid.org/0000-0002-3491-1991

Craig M. Brown, NIST Center for Neutron Research, National Institute of Standards and Technology, Gaithersburg, Maryland 20899-6102, United States; Department of Chemical and Biomolecular Engineering, University of Delaware, Newark, Delaware 19716, United States. https://orcid.org/0000-0002-9637-9355

Hui Wu, NIST Center for Neutron Research, National Institute of Standards and Technology, Gaithersburg, Maryland 20899-6102, United States. ORCID: https://orcid.org/0000-0003-0296-5204

Author Credit

Conceptualization: HW; Formal Analysis: HAE, HW; Investigation: HAE, MC, WZ, TY, CMB, HW; Project administration: HW; Visualization: HAE; Writing – original draft: HAE, HW; Writing – review and editing: HAE, MC, WZ, TY, CMB, HW.

Funding Sources

This research was funded by the National Institute of Standards and Technology (ror.org/05xpvk416). Some of the powder X-ray diffraction data were collected on beamline 17-BM at the Advanced Photon Source at the Argonne National Laboratory, which is supported by the U.S. Department of Energy, Office of Science, Office of Basic Energy Sciences under contract DEAC02-06CH11357.

Acknowledgement

We gratefully acknowledge Mr. Juscelino Leão for his tremendous technical assistance in this project.

(1) Reiner, D. M. Learning through a Portfolio of Carbon Capture and Storage Demonstration Projects. *Nat. Energy* **2016**, *1* (1), 1–7. https://doi.org/10.1038/nenergy.2015.11.
(2) Bui, M.; Adjiman, C. S.; Bardow, A.; Anthony, E. J.; Boston, A.; Brown, S.; Fennell, P. S.; Fuss, S.; Galindo, A.; Hackett, L. A.; Hallett, J. P.; Herzog, H. J.; Jackson, G.; Kemper, J.; Krevor, S.; Maitland, G. C.; Matuszewski, M.; Metcalfe, I. S.; Petit, C.; Puxty, G.; Reimer, J.; Reiner, D. M.; Rubin, E. S.; Scott, S. A.; Shah, N.; Smit, B.; Trusler, J. P. M.; Webley, P.; Wilcox, J.; Dowell, N. M. Carbon Capture and Storage (CCS): The Way Forward. *Energy Environ. Sci.* **2018**, *11* (5), 1062–1176. https://doi.org/10.1039/C7EE02342A.
(3) Erans, M.; Sanz-Pérez, E. S.; Hanak, D. P.; Clulow, Z.; Reiner, D. M.; Mutch, G. A. Direct Air Capture: Process Technology, Techno-Economic and Socio-Political Challenges. *Energy Environ. Sci.* **2022**, *15* (4), 1360–1405. https://doi.org/10.1039/D1EE03523A.
(4) Rochelle, G. T. Amine Scrubbing for CO_2 Capture. *Science* **2009**, *325* (5948), 1652–1654. https://doi.org/10.1126/science.1176731.
(5) Kim, E. J.; Siegelman, R. L.; Jiang, H. Z. H.; Forse, A. C.; Lee, J.-H.; Martell, J. D.; Milner, P. J.; Falkowski, J. M.; Neaton, J. B.; Reimer, J. A.; Weston, S. C.; Long, J. R. Cooperative Carbon Capture and Steam Regeneration with Tetraamine-Appended Metal–Organic Frameworks. *Science* **2020**, *369* (6502), 392–396. https://doi.org/10.1126/science.abb3976.
(6) Shen, X.; Du, H.; Mullins, R. H.; Kommalapati, R. R. Polyethylenimine Applications in Carbon Dioxide Capture and Separation: From Theoretical Study to Experimental Work. *Energy Technol.* **2017**, *5* (6), 822–833. https://doi.org/10.1002/ente.201600694.
(7) Yamada, H. Amine-Based Capture of CO_2 for Utilization and Storage. *Polym. J.* **2021**, *53* (1), 93–102. https://doi.org/10.1038/s41428-020-00400-y.
(8) Sanz-Pérez, E. S.; Murdock, C. R.; Didas, S. A.; Jones, C. W. Direct Capture of CO_2 from Ambient Air. *Chem. Rev.* **2016**, *116* (19), 11840–11876. https://doi.org/10.1021/acs.chemrev.6b00173.
(9) Liu, Q.; Wu, L.; Jackstell, R.; Beller, M. Using Carbon Dioxide as a Building Block in Organic Synthesis. *Nat. Commun.* **2015**, *6* (1), 5933. https://doi.org/10.1038/ncomms6933.

(10) Lombardo, L.; Yang, H.; Zhao, K.; Dyson, P. J.; Züttel, A. Solvent- and Catalyst-Free Carbon Dioxide Capture and Reduction to Formate with Borohydride Ionic Liquid. *ChemSusChem* **2020**, *13* (8), 2025–2031. https://doi.org/10.1002/cssc.201903514.

(11) Zhu, W.; Zhao, J.; Wang, L.; Teng, Y.-L.; Dong, B.-X. Mechanochemical Reactions of Alkali Borohydride with CO_2 under Ambient Temperature. *J. Solid State Chem.* **2019**, *277*, 828–832. https://doi.org/10.1016/j.jssc.2019.07.037.

(12) Jeong, S.; Milner, P. J.; Wan, L. F.; Liu, Y.-S.; Oktawiec, J.; Zaia, E. W.; Forse, A. C.; Leick, N.; Gennett, T.; Guo, J.; Prendergast, D.; Long, J. R.; Urban, J. J. Runaway Carbon Dioxide Conversion Leads to Enhanced Uptake in a Nanohybrid Form of Porous Magnesium Borohydride. *Adv. Mater.* **2019**, *31* (44), 1904252. https://doi.org/10.1002/adma.201904252.

(13) Lombardo, L.; Ko, Y.; Zhao, K.; Yang, H.; Züttel, A. Direct CO_2 Capture and Reduction to High-End Chemicals with Tetraalkylammonium Borohydrides. *Angew. Chem. Int. Ed.* **2021**, *60* (17), 9580–9589. https://doi.org/10.1002/anie.202100447.

(14) Zhao, Y.; Zhang, Z.; Qian, X.; Han, Y. Properties of Carbon Dioxide Absorption and Reduction by Sodium Borohydride under Atmospheric Pressure. *Fuel* **2015**, *142*, 1–8. https://doi.org/10.1016/j.fuel.2014.10.070.

(15) Evans, H. A.; Mullangi, D.; Deng, Z.; Wang, Y.; Peh, S. B.; Wei, F.; Wang, J.; Brown, C. M.; Zhao, D.; Canepa, P.; Cheetham, A. K. Aluminum Formate, $Al(HCOO)_3$: An Earth-Abundant, Scalable, and Highly Selective Material for CO_2 Capture. *Sci. Adv.* **2022**, *8* (44), eade1473. https://doi.org/10.1126/sciadv.ade1473.

(16) Wang, S.; Yan, S.; Ma, X.; Gong, J. Recent Advances in Capture of Carbon Dioxide Using Alkali-Metal-Based Oxides. *Energy Environ. Sci.* **2011**, *4* (10), 3805–3819. https://doi.org/10.1039/C1EE01116B.

(17) Zhang, H.; Goeppert, A.; Prakash, G. K. S.; Olah, G. Applicability of Linear Polyethylenimine Supported on Nano-Silica for the Adsorption of CO_2 from Various Sources Including Dry Air. *RSC Adv.* **2015**, *5* (65), 52550–52562. https://doi.org/10.1039/C5RA05428A.

(18) Varghese, A. M.; Karanikolos, G. N. CO_2 Capture Adsorbents Functionalized by Amine – Bearing Polymers: A Review. *Int. J. Greenh. Gas Control* **2020**, *96*, 103005. https://doi.org/10.1016/j.ijggc.2020.103005.

(19) Wijesiri, R. P.; Knowles, G. P.; Yeasmin, H.; Hoadley, A. F. A.; Chaffee, A. L. CO_2 Capture from Air Using Pelletized Polyethylenimine Impregnated MCF Silica. *Ind. Eng. Chem. Res.* **2019**, *58* (8), 3293–3303. https://doi.org/10.1021/acs.iecr.8b04973.

(20) Quang, D. V.; Soukri, M.; Tanthana, J.; Sharma, P.; Nelson, T. O.; Lail, M.; Coleman, L. J. I.; Abu-Zahra, M. R. M. Investigation of CO_2 Adsorption Performance and Fluidization Behavior of Mesoporous Silica Supported Polyethyleneimine. *Powder Technol.* **2016**, *301*, 449–462. https://doi.org/10.1016/j.powtec.2016.06.027.

(21) Nelson, T. O.; Kataria, A.; Mobley, P.; Soukri, M.; Tanthana, J. RTI's Solid Sorbent-Based CO_2 Capture Process: Technical and Economic Lessons Learned for Application in Coal-Fired, NGCC, and Cement Plants. *Energy Procedia* **2017**, *114*, 2506–2524. https://doi.org/10.1016/j.egypro.2017.03.1409.

(22) Li, K.; Jiang, J.; Yan, F.; Tian, S.; Chen, X. The Influence of Polyethyleneimine Type and Molecular Weight on the CO_2 Capture Performance of PEI-Nano Silica Adsorbents. *Appl. Energy* **2014**, *136*, 750–755. https://doi.org/10.1016/j.apenergy.2014.09.057.

(23) Drage, T. C.; Arenillas, A.; Smith, K. M.; Snape, C. E. Thermal Stability of Polyethylenimine Based Carbon Dioxide Adsorbents and Its Influence on Selection of Regeneration Strategies. *Microporous Mesoporous Mater.* **2008**, *116* (1), 504–512. https://doi.org/10.1016/j.micromeso.2008.05.009.

(24) Celedonio, J. M.; Park, J. H.; Ko, Y. S. FT-IR Study on CO_2 Adsorbed Species of CO_2 Sorbents. *Res. Chem. Intermed.* **2016**, *42* (1), 141–154. https://doi.org/10.1007/s11164-015-2382-x.

(25) Sayari, A.; Heydari-Gorji, A.; Yang, Y. CO_2-Induced Degradation of Amine-Containing Adsorbents: Reaction Products and Pathways. *J. Am. Chem. Soc.* **2012**, *134* (33), 13834–13842. https://doi.org/10.1021/ja304888a.

(26) Zhang, S.; He, L.-N. Capture and Fixation of CO_2 Promoted by Guanidine Derivatives. *Aust. J. Chem.* **2014**, *67* (7), 980–988. https://doi.org/10.1071/CH14125.

(27) Seipp, C. A.; Williams, N. J.; Kidder, M. K.; Custelcean, R. CO_2 Capture from Ambient Air by Crystallization with a Guanidine Sorbent. *Angew. Chem. Int. Ed.* **2017**, *56* (4), 1042–1045. https://doi.org/10.1002/anie.201610916.

(28) Wang, C.; Mahurin, S. M.; Luo, H.; Baker, G. A.; Li, H.; Dai, S. Reversible and Robust CO_2 Capture by Equimolar Task-Specific Ionic Liquid–Superbase Mixtures. *Green Chem.* **2010**, *12* (5), 870–874. https://doi.org/10.1039/B927514B.

(29) Williams, N. J.; Seipp, C. A.; Brethomé, F. M.; Ma, Y.-Z.; Ivanov, A. S.; Bryantsev, V. S.; Kidder, M. K.; Martin, H. J.; Holguin, E.; Garrabrant, K. A.; Custelcean, R. CO_2 Capture via Crystalline Hydrogen-Bonded Bicarbonate Dimers. *Chem* **2019**, *5* (3), 719–730. https://doi.org/10.1016/j.chempr.2018.12.025.

(30) Brethomé, F. M.; Williams, N. J.; Seipp, C. A.; Kidder, M. K.; Custelcean, R. Direct Air Capture of CO_2 via Aqueous-Phase Absorption and Crystalline-Phase Release Using Concentrated Solar Power. *Nat. Energy* **2018**, *3* (7), 553–559. https://doi.org/10.1038/s41560-018-0150-z.

(31) Cai, H.; Zhang, X.; Lei, L.; Xiao, C. Direct CO_2 Capture from Air via Crystallization with a Trichelating Iminoguanidine Ligand. *ACS Omega* **2020**, *5* (32), 20428–20437. https://doi.org/10.1021/acsomega.0c02460.

(32) Garrabrant, K. A.; Williams, N. J.; Holguin, E.; Brethomé, F. M.; Tsouris, C.; Custelcean, R. Energy-Efficient CO_2 Capture from Flue Gas by Absorption with Amino Acids and Crystallization with a Bis-Iminoguanidine. *Ind. Eng. Chem. Res.* **2019**, *58* (24), 10510–10515. https://doi.org/10.1021/acs.iecr.9b00954.

(33) Alkhabbaz, M. A.; Khunsupat, R.; Jones, C. W. Guanidinylated Poly(Allylamine) Supported on Mesoporous Silica for CO_2 Capture from Flue Gas. *Fuel* **2014**, *121*, 79–85. https://doi.org/10.1016/j.fuel.2013.12.018.

(34) Sabet-Sarvestani, H.; Eshghi, H.; Izadyar, M. A Theoretical Study on the Efficiency and Role of Guanidines-Based Organic Superbases on Carbon Dioxide Utilization in Quinazoline-2,4(1H, 3H)-Diones Synthesis. *Struct. Chem.* **2017**, *28* (3), 675–686. https://doi.org/10.1007/s11224-016-0842-6.

(35) Santos, T. C. dos; Bourrelly, S.; Llewellyn, P. L.; Carneiro, J. W. de M.; Ronconi, C. M. Adsorption of CO_2 on Amine-Functionalised MCM-41: Experimental and Theoretical Studies. *Phys. Chem. Chem. Phys.* **2015**, *17* (16), 11095–11102. https://doi.org/10.1039/C5CP00581G.

(36) Park, S. J.; Lee, J. J.; Hoyt, C. B.; Kumar, D. R.; Jones, C. W. Silica Supported Poly(Propylene Guanidine) as a CO_2 Sorbent in Simulated Flue Gas and Direct Air Capture. *Adsorption* **2020**, *26* (1), 89–101. https://doi.org/10.1007/s10450-019-00171-w.

(37) Lee, H. M.; Youn, I. S.; Saleh, M.; Lee, J. W.; Kim, K. S. Interactions of CO_2 with Various Functional Molecules. *Phys. Chem. Chem. Phys.* **2015**, *17* (16), 10925–10933. https://doi.org/10.1039/C5CP00673B.

(38) Anila, S.; Suresh, C. H. Guanidine as a Strong CO_2 Adsorbent: A DFT Study on Cooperative CO_2 Adsorption. *Phys. Chem. Chem. Phys.* **2021**, *23* (24), 13662–13671. https://doi.org/10.1039/D1CP00754H.

(39) Zhou, X.; Zhou, W.; Udovic, T. J.; Yildirim, T.; Rush, J. J.; Rodriguez, E. E.; Wu, H. Development of Potential Organic-Molecule-Based Hydrogen Storage Materials: Converting CN Bond-Breaking Thermolysis of Guanidine to NH Bond-Breaking Dehydrogenation. *Int. J. Hydrog. Energy* **2016**, *41* (41), 18542–18549. https://doi.org/10.1016/j.ijhydene.2016.08.129.

(40) Zhou, W.; Wu, H.; Hartman, M. R.; Yildirim, T. Hydrogen and Methane Adsorption in Metal−organic Frameworks: A High-Pressure Volumetric Study. *J. Phys. Chem. C* **2007**, *111* (44), 16131–16137. https://doi.org/10.1021/jp074889i.

(41) Coelho, A. A. TOPAS and TOPAS-Academic: An Optimization Program Integrating Computer Algebra and Crystallographic Objects Written in C++. *J. Appl. Crystallogr.* **2018**, *51* (1), 210–218. https://doi.org/10.1107/S1600576718000183.

(42) Toby, B. H.; Von Dreele, R. B. GSAS-II: The Genesis of a Modern Open-Source All Purpose Crystallography Software Package. *J. Appl. Crystallogr.* **2013**, *46* (2), 544–549. https://doi.org/10.1107/S0021889813003531.

(43) Wu, H.; Zhou, X.; Rodriguez, E. E.; Zhou, W.; Udovic, T. J.; Yildirim, T.; Rush, J. J. A New Family of Metal Borohydride Guanidinate Complexes: Synthesis, Structures and Hydrogen-Storage Properties. *J. Solid State Chem.* **2016**, *242*, 186–192. https://doi.org/10.1016/j.jssc.2016.07.013.

(44) Liu, Q.; Shi, J.; Zheng, S.; Tao, M.; He, Y.; Shi, Y. Kinetics Studies of CO_2 Adsorption/Desorption on Amine-Functionalized Multiwalled Carbon Nanotubes. *Ind. Eng. Chem. Res.* **2014**, *53* (29), 11677–11683. https://doi.org/10.1021/ie502009n.

(45) Serna-Guerrero, R.; Sayari, A. Modeling Adsorption of CO_2 on Amine-Functionalized Mesoporous Silica. 2: Kinetics and Breakthrough Curves. *Chem. Eng. J.* **2010**, *161* (1), 182–190. https://doi.org/10.1016/j.cej.2010.04.042.

(46) Shirzad, K.; Viney, C. A Critical Review on Applications of the Avrami Equation beyond Materials Science. *J. R. Soc. Interface* **2023**, *20* (203), 20230242. https://doi.org/10.1098/rsif.2023.0242.

(47) Lelito, J. Crystallization Kjinetics Analysis of the Amorphouse $Mg_{72}Zn_{24}Ca_4$ Alloy at the Isothermal Annealing Temperature of 507 K. *Materials* **2020**, *13* (12), 2815. https://doi.org/10.3390/ma13122815.

(48) Marcus, Y. The Guanidinium Ion. *J. Chem. Thermodyn.* **2012**, *48*, 70–74. https://doi.org/10.1016/j.jct.2011.11.031.

(49) Mason, P. E.; Neilson, G. W.; Dempsey, C. E.; Barnes, A. C.; Cruickshank, J. M. The Hydration Structure of Guanidinium and Thiocyanate Ions: Implications for Protein Stability in Aqueous Solution. *Proc. Natl. Acad. Sci. U. S. A.* **2003**, *100* (8), 4557–4561. https://doi.org/10.1073/pnas.0735920100.

(50) Werner, J.; Wernersson, E.; Ekholm, V.; Ottosson, N.; Öhrwall, G.; Heyda, J.; Persson, I.; Söderström, J.; Jungwirth, P.; Björneholm, O. Surface Behavior of Hydrated Guanidinium and Ammonium Ions: A Comparative Study by Photoelectron Spectroscopy and Molecular Dynamics. *J. Phys. Chem. B* **2014**, *118* (25), 7119–7127. https://doi.org/10.1021/jp500867w.

(51) Cooper, R. J.; Heiles, S.; DiTucci, M. J.; Williams, E. R. Hydration of Guanidinium: Second Shell Formation at Small Cluster Size. *J. Phys. Chem. A* **2014**, *118* (30), 5657–5666. https://doi.org/10.1021/jp506429a.